# Polarization independent silicon grating antenna based on subwavelength metamaterials

Sarra Salhi, Xiaochen Xin, Daniel Benedikovic, Carlos Alonso-Ramos, Laurent Vivien, Delphine Marris-Morini, Eric Cassan, Winnie Ye, Daniele Melati

# Polarization independent silicon grating antenna based on subwavelength metamaterials

Sarra Salhi[1,*], Xiaochen Xin[2,*], Daniel Benedikovič[2,3], Carlos Alonso-Ramos [1], Laurent Vivien [1], Delphine Marris-Morini[1], Eric Cassan[1], Winnie N. Ye[2], Daniele Melati [1]

[1]Centre de Nanosciences et de Nanotechnologies, Université Paris-Saclay, CNRS, 91120 Palaiseau, France
[2]Department of Electronics, Carleton University, Ottawa, ON K1S 5B6, Canada
[3]Dept. Multimedia and Information-Communication Technology, University of Zilina, 01026 Zilina, Slovakia

**Abstract**

Optical antennas are key components of an optical phased array system, enabling light coupling between the chip and the free space. In such systems, surface gratings are commonly used as antenna elements, which however suffer from a strong polarization sensitivity of their scattering angle and efficiency. Here, we experimentally demonstrate a surface grating antenna with polarization insensitive behavior on the 500 nm silicon-on-insulator platform exploiting subwavelength metamaterials. The antenna successfully achieves the same diffraction angle of 10° for both TE and TM polarizations, an estimated scattering efficiency of -4 dB, and a difference in diffraction efficiency between the two polarizations smaller than 1 dB over a bandwidth of 31 nm. This antenna facilitates efficient light coupling into and out of photonic integrated circuits.

## 1 Introduction

Optical Phased Arrays (OPAs) for on-chip beam forming and steering represent a promising alternative to traditional mechanically moving components in various applications, notably in light detection and ranging (LiDAR) and free-space optical communications [1–5]. Integrated optical antennas, which are responsible of emitting and receiving light into and from the free space, are the fundamental components of an OPA. Although recent literature demonstrated optical antennas based on metallic structures, dielectric pillars, fiber lenses, photonic crystals and ceramics [6–9], dielectric surface gratings are still the most popular

choice for OPAs because of their relative ease of fabrication and the possibility of achieving high efficiency [10–14]. Surface gratings with high diffraction performances for either transverse-electric (TE) or transverse-magnetic (TM) waveguide modes have been extensively reported in the literature [15–26], especially exploiting L-shaped diffraction elements to break the vertical symmetry and achieve high directionality [18, 27–30]. Grating antennas with specially designed features such as an optimized radiation pattern, improved steerability, and reduced grating lobes have been reported as well [31–34]. Nonetheless, the main drawback of surface gratings is their strong polarization sensitivity, which cause TE and TM modes to be diffracted at different angles and with different efficiencies [35]. The dependence of the optical behavior of the antenna on the polarization of the light often represents a significant challenge, for example in implementing polarization division multiplexing in optical communication systems or ensuring consistent and reliable coupling efficiencies of receiver devices. Polarization sensitivity is particularly pronounced in the high contrast, silicon-on-insulator (SOI) platform commonly used for the development of OPAs because of its strong waveguide birefringence. Nonetheless, optical antennas with a single feeding waveguide capable of effectively supporting both TE and TM polarizations would be extremely beneficial for enhancing the robustness and performance of OPA systems. To overcome this limitation without moving to a different platform or introducing additional materials, subwavelength grating metamaterials (SWG) has been explored in the literature as a promising path [36–39]. SWGs are realized by arranging their unit cells at a distance much smaller than the wavelength, resulting in an effective artificial material whose optical properties can be controlled by modifying the geometry of the unit cells [40]. For example, by exploiting the additional degree of freedom offered by SWG metamaterials, a fiber grating coupler with a difference between TE and TM coupling efficiencies smaller than 1 dB over a bandwidth of 12 nm was experimentally demonstrated in [36] on an air-cladded, suspended membrane waveguide.

In this work, we report on the design and experimental demonstration of an efficient and polarization insensitive grating antenna for free-space coupling based on SWG metamaterials and an L-shaped geometry. The antenna is realized on a 500-nm SOI platform, does not require the removal of the buried oxide, has an oxide top cladding, and a compact footprint of 6.4 $\mu m$ x 2.9 $\mu m$. 3D FDTD simulations show that both TE and TM polarized modes are diffracted with the same scattering angle of 10° with an upward diffraction efficiency of -2.8 dB and -2.4 dB, respectively. The experimental characterization of the antenna, performed with a fiber-based setup, is in good agreement with simulations and demonstrates a difference in TE-TM coupling efficiency at 10° smaller than 1 dB over a 31 nm wavelength range, with an estimated free-space upward scattering efficiency of -4 dB.

# 2 Design of the surface grating antenna

## 2.1 Grating optimization

In order to design the antenna, we start by the diffraction angle of the grating, which can be calculated through the grating equation [38]:

$$\sin(\theta) = \frac{n_B}{n_C} + m\frac{\lambda}{n_C \Lambda_x} \tag{1}$$

where $n_B$ is the effective index of the Bloch mode of the grating, $n_C$ is the refractive index of the cladding material, $\Lambda_x$ is the period of the grating (in the propagation direction x, as defined in Figure 1 (a)) and $\lambda$ is the wavelength, 1550 nm for the design considered here. In order for the TE and TM modes to be diffracted with the same angle, resulting in a polarization insensitive grating, it is required that $n_B$ be the same for the two polarizations, a condition that cannot be generally fulfilled in common SOI gratings. We achieve this objective by incorporating SWG metamaterials into the grating unit cell to engineer the birefringence of the grating waveguide [41]. The grating structure, as schematically represented in Figure 1 (a), includes two sections. The first one is an SWG metamaterial of length of $L_{\mathrm{SWG}}$, with a transverse period in the y direction of $\Lambda_y$ and duty cycle $ff_y$. By adjusting the value of $ff_y$, it is possible to control the equivalent effective refractive index and the birefringence of the metamaterial, as represented in the cross-sectional view of Figure 1 (b). The second section is an L-shaped geometry, partially etched to 50% of the waveguide height for a length of $\mathrm{L}_s$ and with an un-etched part of length $L_u$. The use of an L-shaped geometry is the key to achieve strong directionality and high upward diffraction efficiency [27]. The grating has a total period $\Lambda_x = \mathrm{L_{SWG}} + \mathrm{L}_s + \mathrm{L}_u$ in the propagation direction x. The effective refractive index of the grating Bloch mode can be approximately computed as

$$n_B = (n_{\mathrm{SWG}}\frac{L_{\mathrm{SWG}}}{\Lambda_x}) + (n_s\frac{L_s}{\Lambda_x}) + (n_u\frac{L_u}{\Lambda_x}), \tag{2}$$

where $n_{\mathrm{SWG}}$, $n_s$ and $n_u$ are the effective indices of the fundamental 1-D modes that are supported in the corresponding sections of the unit cell for the polarization of interest, as shown in Figure 1(b). The effective refractive index $n_{\mathrm{SWG}}$ of the SWG section can be changed by changing its duty cycle $ff_y$. To optimize the performance of the antenna, we define two convenient parameters:

$$R_L = \frac{L_s}{L_s + L_u}$$
$$\mathrm{ff}_x = \frac{L_s + L_u}{\Lambda_x},$$

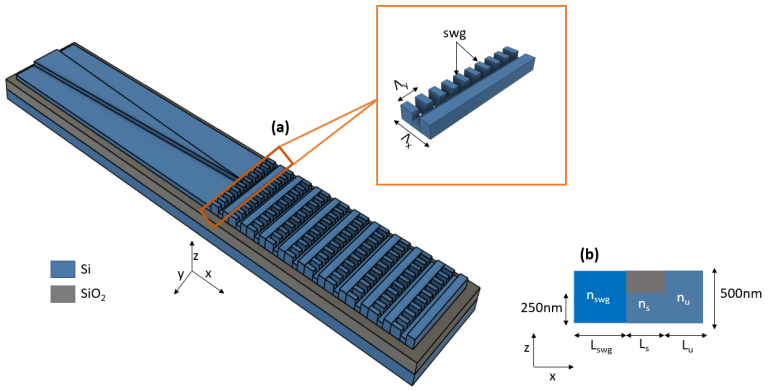


Figure 1: Schematic of the grating antenna. (a) Perspective view and (b) cross section.

being $\mathrm{R}_L$ the duty cycle of the L-shaped geometry only and $\mathrm{ff}_x$ the duty cycle of the entire unit cell of the grating. We then exploit Equation (2) to estimate the Bloch effective indices of both TE and TM modes. For each value of $\mathrm{R}_L$, we computed the grating duty cycle $\mathrm{ff}_x$ which is needed to obtain $\mathrm{n}_B^{\mathrm{TE}} = \mathrm{n}_B^{\mathrm{TM}}$ as a function of the SWG duty cycle $\mathrm{ff}_y$. With this approach, we obtained the curves shown in Figure 2 which represent a set of polarization insensitive designs for the grating. The results are reported for a silicon thickness of both 300 nm and 500 nm. The curves for a silicon thickness of 220 nm are not shown since not only the curves for different values are very close to each other, but all the points on the curves have $\mathrm{ff}_x$ smaller than 0.1. This means that for a typical grating pitch in the range of a couple hundred nanometers, the smallest feature size of the L-shaped region is below 100 nm, which complicates fabrication. We then compute the upward diffraction efficiency $P_{\mathrm{upward}}$ for both polarizations for the different design possibilities reported in Figure 2 using 3D FDTD simulations. The grating periods $\Lambda_x$ of 800 nm and 680 nm were chosen for the 300 nm and 500 nm silicon thickness, respectively, to avoid second order diffraction. Simulation results as a function of $\mathrm{R}_L$ and $\mathrm{ff}_y$ are shown in Figure 3. $P_{\mathrm{upward}}$ for the TE polarized mode shows comparable results between two platforms while the 500 nm silicon thickness has noticeable better performance over the 300 nm silicon for TM polarization. This is caused by the lower confinement of TM polarized light for thinner waveguides which results in less interaction with waveguide perturbations. It was also shown in [22] that it is difficult for thin grating structure to radiate large amount of TM polarized light. The fact that the performance of the grating for TE polarized light hardly further improves aligns with the observation made in [16]. As a result, 500 nm silicon is chosen as the platform for further optimizations. In particular, we sweep the three parameters $R_L$, $ff_y$ and $\Lambda_X$ in order to obtain the highest $P_{\mathrm{upward}}$ for both polarizations simultaneously, considering a fixed buried oxide thickness $t_{\mathrm{BOX}} =$

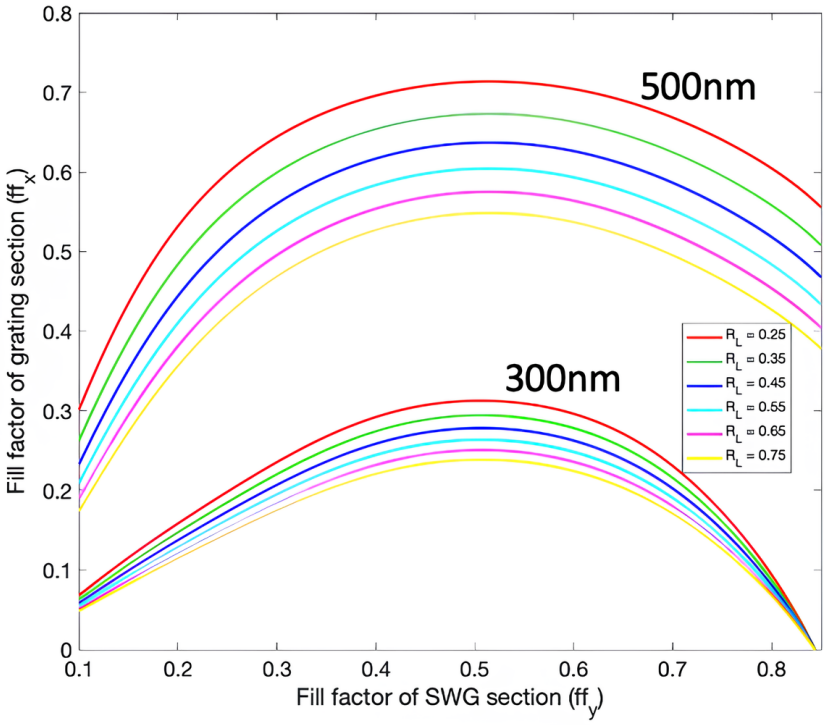


Figure 2: Combinations of $\mathrm{ff}_x$ and $\mathrm{ff}_y$ duty cycles corresponding to polarization-insensitive antenna designs with different $R_L$ for 300 nm and 500 nm silicon thicknesses.

3 $\mu m$, the thickness of the upper cladding $t_{\mathrm{TOX}} = 2.2\ \mu m$ and the period of the SWG metamaterial $\Lambda_Y = 300$ nm. The parameter sweep allows to determine the values as $R_L$=0.45, $ff_y$=0.6 and $\Lambda_x$=643nm. In addition to $P_{\mathrm{upward}}$, one of the most important figures of merits of an antenna is its footprint, which puts constraints on its array integration and directly determines the beamwidth of the far-field (Fraunhofer) pattern through the antenna effective aperture size [42]. The optimization of the antenna's overall length and width involves adjusting the number of diffraction periods in both the x and y directions ($N_x$,$N_y$) to investigate their impact on the far-field beamwidth and the upward diffraction efficiency ($P_{\mathrm{upward}}$). Figure 4 shows the results of the 3D FDTD simulations. As expected, increasing the number of periods in the propagation direction $\mathrm{N}_x$ improves the diffraction efficiency up to the point where no undiffracted light remains in the grating. Likewise, a larger antenna (larger number of transversal SWG periods $\mathrm{N}_y$) improves $P_{\mathrm{upward}}$ by providing a better mode confinement until the effect of the grating lateral sidewalls becomes negligible. Conversely, a larger antenna cause a reduction of the beamwidth in the far field for both azimuth $\phi$ and elevation $\theta$ direction. We chose $N_x$= 10 and $N_y$= 9 as the

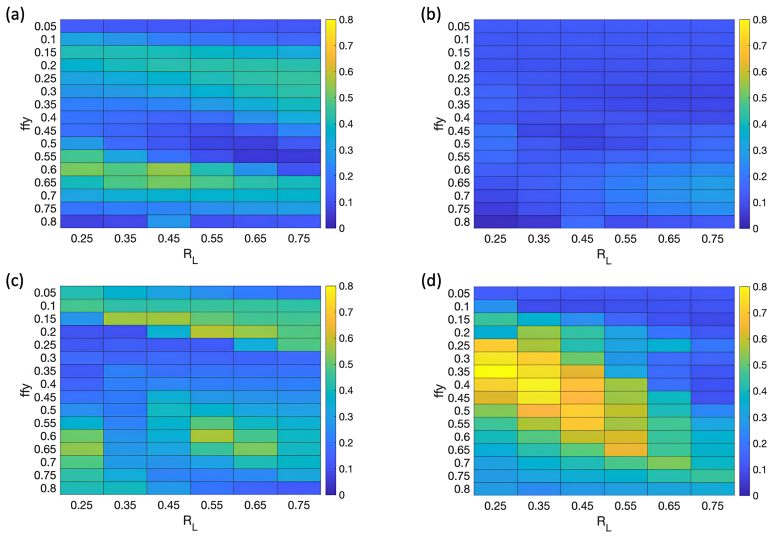


Figure 3: Scattering efficiency $P_{\text{upward}}$ for points along the polarization-insensitive curves of Figure 2. (a) 300 nm silicon, TE mode, (b) 300 nm silicon, TM mode, (c) 500 nm silicon, TE mode, and (d) 500 nm silicon, TM mode.

optimal number of periods ensuring a compact antenna footprint of 6.4 $\mu m$ x 2.9 $\mu m$ with a limited penalty on its efficiency.

## 2.2 Optimization of the injection waveguide

A rib waveguide with an etched depth of 250 nm is used as the input waveguide for the grating because this solution has been proven to effectively reduce back reflection at the grating interface [15]. However, the optimized grating antenna proposed here has an overall width of 2.9 $\mu m$ and it is not practical to have a 2.9 $\mu m$-wide input waveguide while maintaining single mode operation since higher order transverse mode can easily be excited in practice. Therefore, we designed a rib-waveguide-based inverse taper as the input stage of the antenna to connect it with rest of the components on the circuit, as shown in Figure 1(a). Initially, the guided modes are confined in the rib region. As the rib becomes thinner, modes are pushed downward into the slab and then injected into the antenna. The initial width of the inverse taper $w_1$ needs to be properly designed such that only the fundamental TE and TM mode are guided. For the modes to be effectively guided in a rib waveguide, the mode effective indices must be greater than the effective index of the slab $TE_0$ mode [43]. For this reason, an $w_1$ of 500 nm is chosen. The final width $w_2$, on the other hand, has to be chosen to make sure that, at the end of the inverse taper, the modes in the rib waveguide have the best possible overlap with the ideal field excitations of the grating for both polarizations. The ideal excitation fields are defined

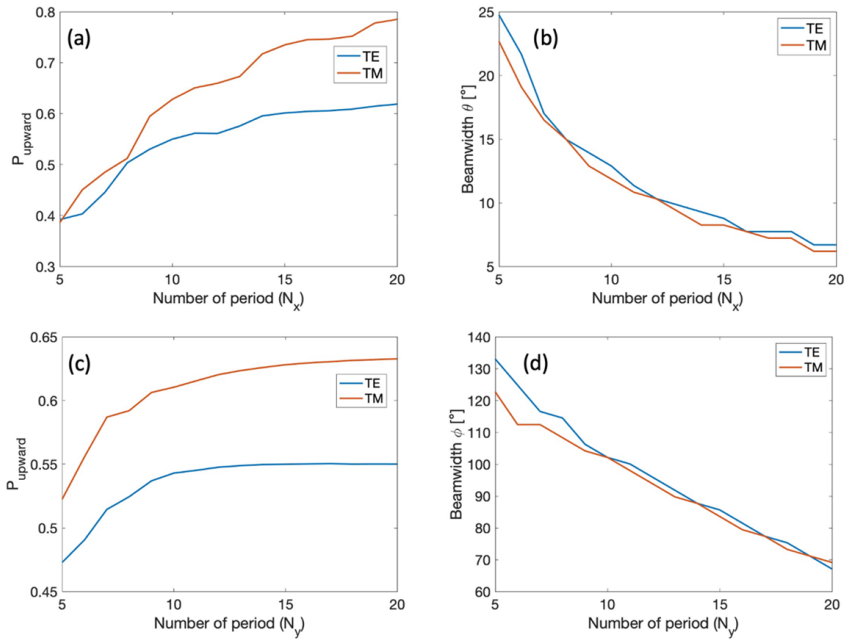


Figure 4: Optimization of the antenna footprint. (a,c) $P_{\text{upward}}$ as a function of the number of periods in the x ($N_x$) and y ($N_y$) directions. (b,d) Beamwidth in the elevation direction $\theta$ and the azimuth direction $\phi$ as a function of $N_x$ and $N_y$

as the $TE_0$ and $TM_0$ mode fields of a 2.9 $\mu m$ wide by 250 nm thick silicon waveguide on an SOI platform with oxide upper cladding. Field overlaps for different rib width $w_2$ for TE and TM are plotted respectively in Figure 5 (a) and (b). As expected, the best overlap occurs with small rib width. $w_2$ of 50 nm is chosen as a good compromise between ease of fabrication and device performance. For comparison, the obtained major electric field component for the two polarizations is plot in the inset alongside with the ideal excitation. Finally, the length of the inverse taper L is optimized such that as much as power is coupled into the desired modes while the length is kept as short as possible. Simulations of power coupling at different taper lengths are performed by extracting the corresponding S-parameter using an Eigen Mode Expansion (EME) solver and the results are shown in Figure 5 (c). L = 11.8 $\mu m$ is selected, which results in estimated power couplings of 92% and 80% for $TE_0$-$TE_0$ and $TM_0$-$TM_0$ transitions respectively.

## 2.3 3D FDTD simulation results

Before proceeding to fabrication, the overall performance of the antenna (including the injection waveguide) were verified using 3D FDTD simulation centered

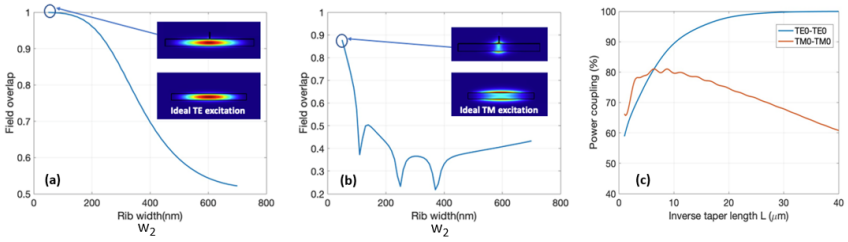


Figure 5: Overlap between the rib waveguide mode and the ideal grating excitation field for (a) the TE and (b) the TM fundamental modes. (c) Power coupling between the input and the output of the injection waveguide as a function of the inverse taper length.

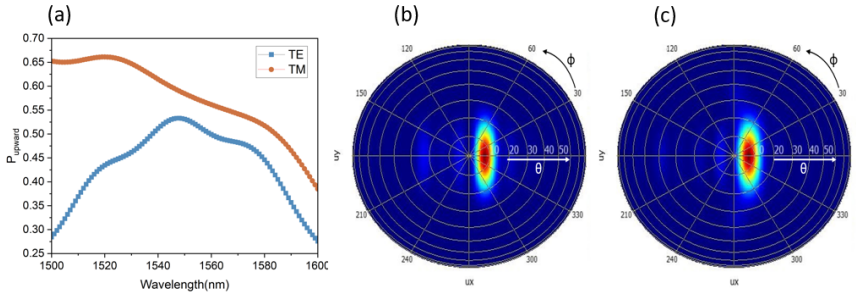


Figure 6: (a) Simulated scattering efficiency for both TE and TM polarizations. (b) Farfield radiation pattern for the TE and (c) the TM modes.

at the desired wavelength of $\lambda$= 1550 nm. Simulation results for the upward diffraction efficiency are shown in Figure 6 (a). As can be seen, the antenna achieves a similar scattering efficiency $P_{\text{upward}}$ of 53% (-2.8 dB) and 58% (-2.4 dB) for TE and TM modes. Since the grating design was the result of a compromise between TE and TM performance at the wavelength of 1550 nm, the antenna achieves even better TM scattering efficiency above 65% for shorter wavelengths. Moreover, as shown by the far field projection of the scattered field in Figure 6 (b) and (c), the grating scattering occurs at an angle of 10° for both polarizations, confirming the polarization insensitive operation. The beamwidth is also the same for both polarizations, being equal to 9° in the elevation direction $\theta$ and 104° in the azimuth direction $\phi$. These findings are also summarized in Table 1.

Table 1: Simulated performance of the designed grating antenna

| | TE | TM |
|---|---|---|
| Diffraction angle | 10° | 10° |
| Upward diffraction efficiency | 53% (-2.8 dB) | 58% (-2.4 dB) |
| Beamwidth ( $\theta$ x $\phi$ ) | 9°x104° | 9.5°x104° |

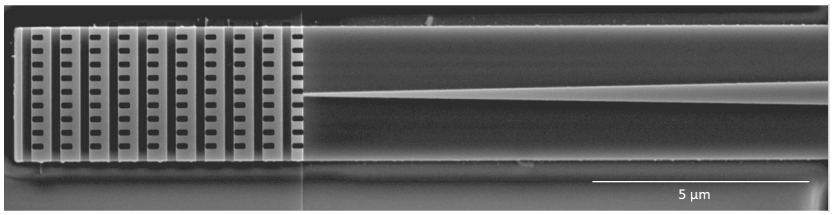


Figure 7: Scanning electron microscopy top view picture of the fabricated grating antenna.

# 3 Grating coupler antenna fabrication and experimental results

In order to experimentally test the performance of our design, the grating antenna was fabricated on a SOI wafer with a silicon layer thickness of 500 nm and a buried oxide layer thickness of 3 $\mu m$. The fabrication process was completed in two steps. Firstly, the SWG metamaterial was created by electron beam lithography, followed by induced coupled plasma (ICP), resulting in a 500 nm etch depth. Next, the partial etched regions in the grating and the rib waveguide were formed using electron beam lithography and ICP etching, achieving a 250 nm etch depth. Finally, we deposited PMMA as the cladding because it has a refractive index similar to that of $SiO_2$ ($n_{\mathrm{PMMA}}$=1.49). A scanning electron microscopy (SEM) image of the fabricated antenna is shown in Figure 7. Two antennas were placed in a back-to-back configuration, connected by a rib waveguide with a length of 5 mm. To facilitate the optical characterization, the scattering efficiency of the antenna was measured using two standard single mode fibers instead of performing direct measurements in free space. The characterization setup is schematically shown in Figure 8. It includes a tunable laser and a polarization controller to set the polarization of the light injected in the grating by the first fiber. 90% of the light collected by the output fiber is sent to the detector while the remaining 10% is fed into a polarimeter. Both input and output fibers have a 10° angle to match the designed emission angle of the antenna. First, light polarization is set to TE using a reference grating with a polarization-dependent transmission realized on the same chip. We then characterize the designed antenna, obtaining the transmission spectrum shown in Figure 9 (a) with a solid blue line. The transmission is normalized to account for both setup losses and the propagation losses of the interconnecting waveguides,

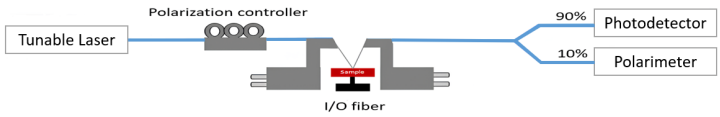


Figure 8: Schematic representation of the experimental setup

which are estimated as 2 dB/cm using an optical frequency domain reflectometry [44]. A peak fiber coupling efficiency of -9 dB is achieved at a wavelength of 1560 nm. We then change the setup polarization to TM using the polarimeter as a reference and measure the normalized transmission spectra shown in Figure 9 (a) with a solid orange line. The same normalization used for TE is applied to TM transmission. In this case, a fiber coupling efficiency of -11.5 dB is obtained at 1560 nm. Figure 9 (b) shows the difference in the fiber coupling efficiency between the TE and TM modes. A perfect polarization-independent operation is achieved at a wavelength of 1532 nm, with a corresponding fiber transmission of -11.5 dB for both TE and TM at this wavelength and a 1-dB polarization insensitive bandwidth of 31 nm.

It should be noted that these results depend on both the upward diffraction efficiency $P_{\text{upward}}$ of the antenna and also on the overlap integral of the scattered field with the fiber mode, which was not considered for the design of an antenna for free-space applications. In order to better evaluate the experimental results, we hence simulate the antenna coupling efficiency with a standard single mode fiber with 3D FDTD for both polarizations. Results are reported in Figure 9 (a) with dashed lines and are in a very good agreement with the experiment. The difference between the experimental fiber transmission and the simulation prediction is smaller than 1 dB for both polarizations in the bandwidth of interest, likely due to fabrication tolerances. In the simulations, a perfect polarization insensitive coupling is obtained at a wavelength of 1538 nm, with coupling efficiency of -10.5 dB. Conservatively assuming that the additional 1 dB loss can be entirely attributed to the scattering efficiency and not to the modes overlap, allows to estimate a $P_{\text{upward}}$ of about -4 dB (40%) for the fabricated antenna for both TE and TM modes.

# 4 Conclusion

We designed and fabricated an insensitive polarization grating antenna in a 500 nm SOI platform. The use of SWG metamaterials was key to obtain the same refractive index for TE and TM grating modes and hence the same scattering angle, while the incorporation of the L-shaped section enhanced the diffraction efficiency. In our experimental demonstration, we successfully achieved a 1-dB polarization insensitive bandwidth of 31 nm with an estimated scattering efficiency of about -4 dB (40%). Our design offers a robust solution for efficiently coupling light into photonic integrated circuits regardless of the polarization

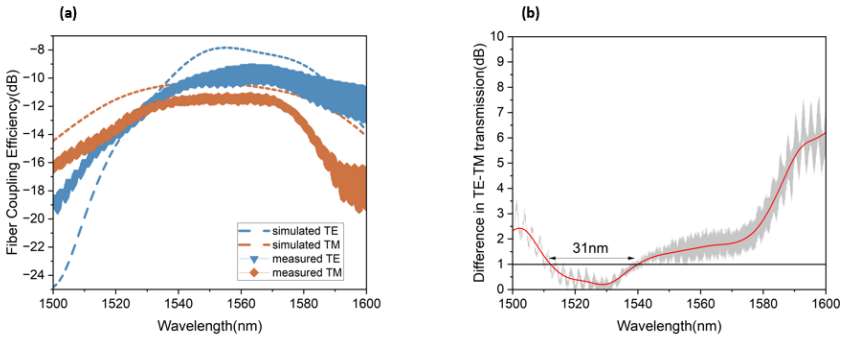


Figure 9: Experimental performance of the grating antenna. (a) Measured (solid lines) and simulated (dashed lines) fiber coupling efficiency for both TE and TM polarizations as a function of the wavelength. (b) Difference in TE-TM measured fiber coupling efficiency.

state. By enabling broadband operation, the antenna holds the potential to realize next-generation photonic applications in telecommunications, data centers, and beyond.

**Acknowledgements** This work was partially funded by the European Union through the European Research Council (ERC) project BEAMS (Grant agreement No.101041131). Views and opinions expressed are however those of the author(s) only and do not necessarily reflect those of the European Union or the European Research Council Executive Agency. Neither the European Union nor the granting authority can be held responsible for them. The device fabrication was performed within the C2N technological platforms and partly supported by the RENATECH network and the General Council of Essonne.

# References

[1] Martijn J.R. Heck. Highly integrated optical phased arrays: Photonic integrated circuits for optical beam shaping and beam steering. *Nanophotonics*, 6(1):93–107, January 2017.

[2] Jelena Notaros, Nanxi Li, Christopher V. Poulton, Zhan Su, Matthew J. Byrd, Emir Salih Magden, Erman Timurdogan, Christopher Baiocco, Nicholas M. Fahrenkopf, and Michael R. Watts. CMOS-Compatible Optical Phased Array Powered by a Monolithically-Integrated Erbium Laser. *Journal of Lightwave Technology*, 37(24):5982–5987, December 2019.

[3] Yongjun Guo, Yuhao Guo, Chunshu Li, Hao Zhang, Xiaoyan Zhou, and Lin Zhang. Integrated Optical Phased Arrays for Beam Forming and Steering. *Applied Sciences*, 11(9):4017, April 2021.

[4] Chao Li, Xianyi Cao, Kan Wu, Gaofeng Qiu, Minglu Cai, Guangjin Zhang, Xinwan Li, and Jianping Chen. Blind zone-suppressed hybrid beam steering for solid-state Lidar. *Photonics Research*, 9(9):1871, September 2021.

[5] David R. Gozzard, Lyle E. Roberts, James T. Spollard, Paul G. Sibley, and Daniel A. Shaddock. Fast beam steering with an optical phased array. *Optics Letters*, 45(13):3793, July 2020.

[6] Chen Sun, Jia Zhao, Jiaheng Wang, and Xiqi Gao. Fiber Lens Based Optical Antenna Design for OWC With Full Beam Coverage. *IEEE Photonics Journal*, 13(6):1–10, December 2021.

[7] Ryo Tetsuya, Takemasa Tamanuki, Riku Kubota, Mikiya Kamata, and Toshihiko Baba. Point Cloud Imaging using Si Photonic Crystal Optical Antenna Serial Array. In *2022 27th OptoElectronics and Communications Conference (OECC) and 2022 International Conference on Photonics in Switching and Computing (PSC)*, pages 1–3, Toyama, Japan, July 2022. IEEE.

[8] Anand Sharma, Ajay Kumar Dwivedi, Nagesh Kallollu Narayaswamy, Yogendra Kumar Prajapati, and Devendra Kumar Tripathi. Ceramic material-based optical antenna for multiband photonics applications. *Optical Engineering*, 61(01), January 2022.

[9] Reza Fatemi, Parham P. Khial, Aroutin Khachaturian, and Ali Hajimiri. Breaking FOV-Aperture Trade-Off With Multi-Mode Nano-Photonic Antennas. *IEEE Journal of Selected Topics in Quantum Electronics*, 27(1):1–14, January 2021.

[10] Jie Sun, Erman Timurdogan, Ami Yaacobi, Ehsan Shah Hosseini, and Michael R. Watts. Large-scale nanophotonic phased array. *Nature*, 493(7431):195–199, January 2013.

[11] Hooman Abediasl and Hossein Hashemi. Monolithic optical phased-array transceiver in a standard SOI CMOS process. *Optics Express*, 23(5):6509, March 2015.

[12] Karel Van Acoleyen, Hendrik Rogier, and Roel Baets. Two-dimensional optical phased array antenna on silicon-on-Insulator. *Optics Express*, 18(13):13655, June 2010.

[13] Chul-Soon Im, Bishal Bhandari, Kyeong-Pyo Lee, Sung-Moon Kim, Min-Cheol Oh, and Sang-Shin Lee. Silicon nitride optical phased array based on a grating antenna enabling wavelength-tuned beam steering. *Optics Express*, 28(3):3270, February 2020.

[14] Reza Fatemi, Behrooz Abiri, Aroutin Khachaturian, and Ali Hajimiri. High sensitivity active flat optics optical phased array receiver with a two-dimensional aperture. *Optics Express*, 26(23):29983, November 2018.

[15] Carlos Alonso-Ramos, Milos Nedeljkovic, Daniel Benedikovic, Jordi Soler Penadés, Callum G. Littlejohns, Ali Z. Khokhar, Diego Pérez-Galacho, Laurent Vivien, Pavel Cheben, and Goran Z. Mashanovich. Germanium-on-silicon mid-infrared grating couplers with low-reflectivity inverse taper excitation. *Optics Letters*, 41(18):4324, September 2016.

[16] Angelo Bozzola, Lee Carroll, Dario Gerace, Ilaria Cristiani, and Lucio Claudio Andreani. Optimising apodized grating couplers in a pure SOI platform to -05 dB coupling efficiency. *Optics Express*, 23(12):16289, June 2015.

[17] Xia Chen and H.K. Tsang. Nanoholes Grating Couplers for Coupling Between Silicon-on-Insulator Waveguides and Optical Fibers. *IEEE Photonics Journal*, 1(3):184–190, September 2009.

[18] Daniel Benedikovic, Pavel Cheben, Jens H. Schmid, Dan-Xia Xu, Jean Lapointe, Shurui Wang, Robert Halir, Alejandro Ortega-Moñux, Siegfried Janz, and Milan Dado. High-efficiency single etch step apodized surface grating coupler using subwavelength structure. *Laser & Photonics Reviews*, 8(6), November 2014.

[19] Yun Wang, Wei Shi, Xu Wang, Zeqin Lu, Michael Caverley, Richard Bojko, Lukas Chrostowski, and Nicolas A. F. Jaeger. Design of broadband subwavelength grating couplers with low back reflection. *Optics Letters*, 40(20):4647, October 2015.

[20] Galina Georgieva, Karsten Voigt, Anna Peczek, Christian Mai, and Lars Zimmermann. Design and performance analysis of integrated focusing grating couplers for the transverse-magnetic TM00 mode in a photonic BiCMOS technology. *Journal of the European Optical Society-Rapid Publications*, 16(1):7, December 2020.

[21] G. Georgieva, K. Voigt, and L. Zimmermann. Focusing 1D Silicon Photonic Grating Coupler in Photonic BiCMOS Technology for the Excitation of the Fundamental TM Mode. In *2019 PhotonIcs & Electromagnetics Research Symposium - Spring (PIERS-Spring)*, pages 1667–1673, Rome, Italy, June 2019. IEEE.

[22] Robert Halir, Pavel Cheben, Siegfried Janz, Dan-Xia Xu, Íñigo Molina-Fernández, and Juan G. Wangüemert-Pérez. Waveguide grating coupler with subwavelength microstructures. *Optics Letters*, 34(9):1408, May 2009.

[23] Jun Zou, Yang Zhang, Jinhua Hu, Changhui Wang, Ming Zhang, and Zichun Le. Grating Coupler With Reduced Back Reflection Using $\lambda$ /4 Offset at Its Grating Sub-Teeth. *Journal of Lightwave Technology*, 37(4):1195–1199, February 2019.

[24] Jahn Hoffmann, K. Marvin Schulz, Giampaolo Pitruzzello, Lena Simone Fohrmann, Alexander Yu. Petrov, and Manfred Eich. Backscattering design for a focusing grating coupler with fully etched slots for transverse magnetic modes. *Scientific Reports*, 8(1):17746, December 2018.

[25] R. Halir, P. Cheben, J. H. Schmid, R. Ma, D. Bedard, S. Janz, D.-X. Xu, A. Densmore, J. Lapointe, and Í. Molina-Fernández. Continuously apodized fiber-to-chip surface grating coupler with refractive index engineered subwavelength structure. *Optics Letters*, 35(19):3243, October 2010.

[26] Jian Kang, Zhenzhou Cheng, Wen Zhou, Ting-Hui Xiao, Kimmy-Laure Gopalakrisna, Mitsuru Takenaka, Hon Ki Tsang, and Keisuke Goda. Focusing subwavelength grating coupler for mid-infrared suspended membrane germanium waveguides. *Optics Letters*, 42(11):2094, June 2017.

[27] Daniel Benedikovic, Carlos Alonso-Ramos, Diego Pérez-Galacho, Sylvain Guerber, Vladyslav Vakarin, Guillaume Marcaud, Xavier Le Roux, Eric Cassan, Delphine Marris-Morini, Pavel Cheben, Frédéric Boeuf, Charles Baudot, and Laurent Vivien. L-shaped fiber-chip grating couplers with high directionality and low reflectivity fabricated with deep-UV lithography. *Optics Letters*, 42(17):3439, September 2017.

[28] Mohsen Kamandar Dezfouli, Yuri Grinberg, Daniele Melati, Pavel Cheben, Jens H. Schmid, Alejandro Sánchez-Postigo, Alejandro Ortega-Moñux, Gonzalo Wangüemert-Pérez, Ross Cheriton, Siegfried Janz, and Dan-Xia Xu. Perfectly vertical surface grating couplers using subwavelength engineering for increased feature sizes. *Optics Letters*, 45(13):3701, July 2020.

[29] Qiankun Liu, Daniel Benedikovic, Tom Smy, Ahmad Atieh, Pavel Cheben, and Winnie N. Ye. Circular Optical Phased Arrays with Radial Nano-Antennas. *Nanomaterials*, 12(11):1938, June 2022.

[30] Daniele Melati, Mohsen Kamandar Dezfouli, Yuri Grinberg, Jens H. Schmid, Ross Cheriton, Siegfried Janz, Pavel Cheben, and Dan-Xia Xu. Design of Compact and Efficient Silicon Photonic Micro Antennas with Perfectly Vertical Emission. *IEEE Journal of Selected Topics in Quantum Electronics*, 27(1):1–10, July 2020.

[31] Reza Fatemi, Aroutin Khachaturian, and Ali Hajimiri. A Nonuniform Sparse 2-D Large-FOV Optical Phased Array With a Low-Power PWM Drive. *IEEE Journal of Solid-State Circuits*, 54(5):1200–1215, May 2019.

[32] Shahrzad Khajavi, Daniele Melati, Pavel Cheben, Jens H. Schmid, Carlos A. Alonso Ramos, and Winnie N. Ye. Highly efficient ultra-broad beam silicon nanophotonic antenna based on near-field phase engineering. *Scientific Reports*, 12(1):18808, November 2022.

[33] J. K. Doylend, M. J. R. Heck, J. T. Bovington, J. D. Peters, L. A. Coldren, and J. E. Bowers. Two-dimensional free-space beam steering with an optical phased array on silicon-on-insulator. *Optics Express*, 19(22):21595, October 2011.

[34] P. F. Wang, G. Z. Luo, H. Y. Yu, Y. J. Li, M. Q. Wang, X. L. Zhou, W. X. Chen, Y. J. Zhang, and J. Q. Pan. Improving the performance of optical

antenna for optical phased arrays through high-contrast grating structure on SOI substrate. *Optics Express*, 27(3):2703, February 2019.

[35] D. Taillaert, Harold Chong, P.I. Borel, L.H. Frandsen, R.M. De La Rue, and R. Baets. A compact two-dimensional grating coupler used as a polarization splitter. *IEEE Photonics Technology Letters*, 15(9):1249–1251, September 2003.

[36] Zhenzhou Cheng and Hon Ki Tsang. Experimental demonstration of polarization-insensitive air-cladding grating couplers for silicon-on-insulator waveguides. *Optics Letters*, 39(7):2206, April 2014.

[37] Yun Wang, Xu Wang, Jonas Flueckiger, Han Yun, Wei Shi, Richard Bojko, Nicolas A. F. Jaeger, and Lukas Chrostowski. Focusing sub-wavelength grating couplers with low back reflections for rapid prototyping of silicon photonic circuits. *Optics Express*, 22(17):20652, August 2014.

[38] Tianyi Hao, Alejandro Sanchez-Postigo, Pavel Cheben, Alejandro Ortega-Monux, and Winnie N. Ye. Dual-Band Polarization-Independent Subwavelength Grating Coupler for Wavelength Demultiplexing. *IEEE Photonics Technology Letters*, 32(18):1163–1166, September 2020.

[39] Xia Chen and Hon K. Tsang. Polarization-independent grating couplers for silicon-on-insulator nanophotonic waveguides. *Optics Letters*, 36(6):796, March 2011.

[40] Pavel Cheben, Jens H. Schmid, Robert Halir, José Manuel Luque-González, J. Gonzalo Wangüemert-Pérez, Daniele Melati, and Carlos Alonso-Ramos. Recent advances in metamaterial integrated photonics. *Advances in Optics and Photonics*, 15(4):1033–1105, December 2023.

[41] Xiaochen Xin, Daniel Benedikovic, and Winnie N. Ye. Silicon-based polarization-insensitive optical antennas. In Sonia M. García-Blanco and Pavel Cheben, editors, *Integrated Optics: Devices, Materials, and Technologies XXVII*, page 59, San Francisco, United States, March 2023. SPIE.

[42] Grant R. Fowles. *Introduction to Modern Optics*. Dover Publications, New York, 2nd ed., dover ed edition, 1989.

[43] Xuejun Xu, Shaowu Chen, Jinzhong Yu, and Xiaoguang Tu. An investigation of the mode characteristics of SOI submicron rib waveguides using the film mode matching method. *Journal of Optics A: Pure and Applied Optics*, 11(1):015508, January 2009.

[44] D. Melati, A. Alippi, and A. Melloni. Waveguide-Based Technique for Wafer-Level Measurement of Phase and Group Effective Refractive Indices. *Journal of Lightwave Technology*, 34(4):1293–1299, February 2016.